

## Characterizing urban land changes of 30 global megacities using nighttime light time series stacks

Qiming Zheng<sup>a,b,c</sup>, Qihao Weng<sup>b,\*</sup>, Ke Wang<sup>c</sup>

<sup>a</sup> Centre for Nature-based Climate Solutions, Department of Biological Sciences, National University of Singapore, 16 Science Drive 4, Singapore 117558, Singapore

<sup>b</sup> Center for Urban and Environmental Change, Department of Earth and Environmental Systems, Indiana State University, Terre Haute, IN 47809, USA

<sup>c</sup> Institute of Applied Remote Sensing and Information Technology, College of Environmental and Resource Sciences, Zhejiang University, Hangzhou, Zhejiang 310058, China

### ARTICLE INFO

#### Keywords:

Nighttime light imagery  
Land use and land cover changes  
Urbanization  
Time series analysis  
Megacities  
Urban areas  
Sustainability

### ABSTRACT

Worldwide urbanization has brought about diverse types of urban land use and land cover (LULC) changes. The diversity of urban land changes, however, have been greatly under studied, since the major focus of past research has been on urban growth. In this study, we proposed a framework to characterize diverse urban land changes of 30 global megacities using monthly nighttime light time series from VIIRS data. First, we developed a Logistic-Harmonic model to fit VIIRS time series. Second, by leveraging the uniqueness of urban land change and nighttime light data, we incorporated temporal information of VIIRS time series and proposed a new classification scheme to produce monthly maps of built-up areas and to disentangle urban land changes into five categories. Third, we provided an in-depth analysis and comparison of urban land change patterns of the selected megacities. Results demonstrated that the Logistic-Harmonic model yielded a robust performance in fitting VIIRS time series. Temporal features based classification can not only significantly improve the mapping accuracy of built-up areas, especially for regions with heterogeneous built-up and non-built-up landscapes, but also promoted temporal consistency and classification efficiency. Urban land changes occurred in 51% of the built-up pixels of the megacities. Compared with urban growth, other types of urban land change, particularly land use intensification, contributed to an unexpectedly large proportion of the changes (83%). The findings of this study offer an insightful understanding on global urbanization processes in megacities, and evoke further investigation on the environmental and ecological implications of urban land changes.

### 1. Introduction

The world population, as reported by World Population Prospects 2019, is increasing towards 9.7 billion in 2050 ([United Nations, 2019](#)). The ongoing urbanization is projected to account for about 26% (2.5 billion) of the growth, whilst the urban dwellers will increase from 55% to 68% of the overall world's population by 2050 ([United Nations, 2018](#)).

This dramatic demographic transition, shifting population from rural to urban, is bringing a substantial of sophisticated and diverse changes to urban land, both in land use and land cover (LULC). The knowledge of how diverse urban changes are unfolded and progressed is of high significance to the understanding of urban environment and socio-economic changes. It has been well-documented that urban land changes have triggered a succession of repercussions on local

environment, human health and global climate ([Seto et al., 2012](#)). Monitoring urban changes in a spatially explicit and temporally intensive manner provides essential information for addressing these environmental issues. Understanding urban land changes is closely pertinent to the focus of Sustainable Development Goals 11, making cities and human settlement sustainable ([Griggs et al., 2013](#)), which requires information on urban land use and land cover, urban form and growth patterns, slums, buildings, transportation and infrastructure, green and public spaces, cultural and natural heritage sites.

These demands pose new opportunities and challenges, requiring new geospatial techniques in characterizing different types of urban land changes. "Daytime" remote sensing imageries, like Landsat or MODIS, mainly present the biophysical attribute of earth's surface. Previous studies with "daytime" remote sensing imagery thus have focused efforts on tracking a single type of urban land change, i.e.,

\* Corresponding author.

E-mail address: [qweng@indstate.edu](mailto:qweng@indstate.edu) (Q. Weng).

growth of urban extents (Song et al., 2018; Zhu et al., 2019). Such unidimensional measurement greatly underrepresents the other types of urban land changes, such as urban land use intensification and deurbanization. Previous attempts, such as using population density grid (van Vliet et al., 2019) and volumetric growth estimated from microwave backscatter data (Mahta et al., 2019), measure urban land use intensity from a single dimension, while urban land use change per se is a sophisticated process. Geospatial big-data, such as social media and Point-of-Interests (POIs) data, have been widely used for measuring the socio-economic attributes and quantify human activities intensity (Li et al., 2016). However, its potential for uncovering urban land use changes is constrained due to the limited spatial and temporal data coverage, as well as a biased representation. Yet, it is imperative to develop further understanding of the spatiotemporal characteristics of different types of urban land changes of global megacities.

Nighttime light (NTL) imagery, including the Defense Meteorological Program Operational Line-Scan System (DMSP-OLS) and the Visible Infrared Imaging Radiometer Suite (VIIRS) of Suomi-NPP, provides unique optical remote sensing data and is able to detect artificial lights emitted from urban areas at night, reflecting both human settlements and activities (Elvidge et al., 2013; Levin et al., 2020; Román et al., 2018). NTL data has been extensively used for mapping urban built-up areas (Imhoff et al., 1997; Zhou et al., 2018) and characterizing urban land use intensity due to its high correlation with built-up area density and height (Elvidge et al., 2017; Estrada-García et al., 2016; Levin, 2017) and socio-economic variables, such as, population density and energy consumption (Zhao et al., 2018a). The detected NTL intensity thereby has a great potential for characterizing and mapping different types of urban land changes.

From the perspective mapping urban land changes, the full potential of NTL time series has yet to be explored. For the bulk of NTL based applications, only spectral information, i.e., NTL intensity, is used. These studies are carried out at an annual basis, using either the annual composite DMSP-OLS or annual averaged NTL intensity aggregated from monthly VIIRS data (Xie and Weng, 2017; Zhao et al., 2018b). In this way, urban land changes happening in a short period of time would be buried in annual time series and is untraceable. In contrast, temporal information that is beneficial to LULC classification accuracy is greatly underutilized in existing NTL-based applications.

In this study, we present a new framework to identify and characterize different types of urban land change of global megacities using

monthly VIIRS time series data. The specific objectives of our study are threefold: (i) to develop a Logistic-Harmonic model to fit monthly VIIRS time series; (ii) to generate monthly built-up maps and disentangle different urban land change types; and (iii) to analyze urban land change patterns of 30 global megacities.

## 2. Study area and datasets

Thirty megacities were selected as the study areas to represent megacities of a wide variety of backgrounds, including urbanization degree (e.g., size and population), climate conditions and landscape configuration (Fig. 1). These megacities are representatives of urbanization hotspots in the past and the near future in terms of current population and projected population by 2030 (GaWC, 2018; United Nations, 2016). Tracking urban land changes of these megacities are crucial as it provides information regarding how global urbanization has been unfolding, and underpins the future development planning for their less urbanized counterparts. At the same time, it is worth noting that stray lights at high latitude and frequent cloud coverage at low latitude regions have a strong impact on the quality of monthly VIIRS data. Megacities located at tropical and sub-frigid areas, such as Kuala Lumpur ( $3^{\circ}\text{N}$ ) and Moscow ( $55^{\circ}\text{N}$ ) were thus deliberately selected to examine the robustness of the proposed method. Further, we provided a glimpse into how our method can be applied to medium-size cities (see Appendix A1).

The Version 1 monthly averaged VIIRS time series images, 84 months in total, from April 2012 to March 2019, were used to map the urban land changes. VIIRS image has a 15 arc sec spatial resolution, an NTL detection capability of large dynamic range (14 bit) and sensitive low light detection limit ( $2 \times 10^{-11} \text{ W/cm}^2/\text{sr}$ ) (Elvidge et al., 2017). This VIIRS data is a monthly composite product, presenting the mean radiance of all valid cloud-free observations in a month. It comprises two data sets: (1) average radiance (avg\_rad) and (2) number of cloud free observations (cf\_cvg) used for calculating the avg\_rad. We resampled VIIRS to 500-m spatial resolution. In addition, Collection 6 MODIS 16-Day NDVI (MOD13A1, 500 m) and annual land cover maps (MCD12Q1, 500 m), and Global Human Settlement Layer (GHSL), a 30-m resolution urban footprint map (Pesaresi et al., 2013), were pre-processed and downloaded for use in Google Earth Engine platform.

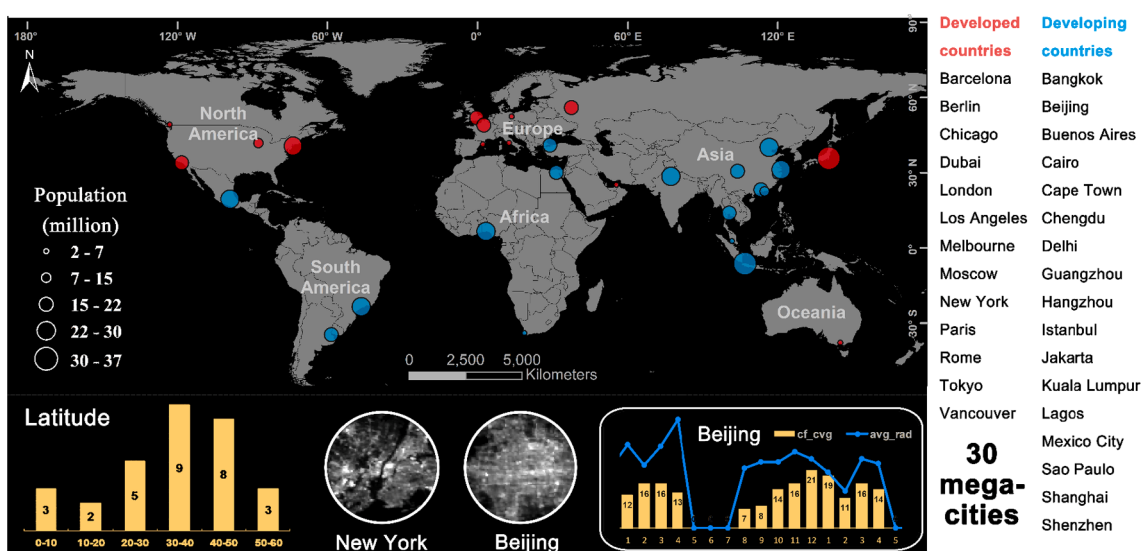


**Fig. 1.** Study areas: 30 global megacities. The bottom-left histogram summarizes latitude of selected megacities. The zoom-in diagram at the bottom-right corner is a VIIRS pixel time series of different months in Beijing, where the histogram and the blue line indicate the average radiance (avg\_rad) and the number of cloud free observations (cf\_cvg), respectively. (For interpretation of the references to colour in this figure legend, the reader is referred to the web version of this article.)

### 3. Methodology

#### 3.1. Overview

Fig. 2 shows a schematic flowchart of the proposed analytical framework. In this study, urban land change process is modelled and described as a whole process. Based on this point, we proposed a Logistic-Harmonic model to fit VIIRS time series (Section 3.2), and a classification scheme to disentangle urban land change into five types (Section 3.3), including: (i) **urban growth**, the conversion in the biophysical property of land cover, where natural landscapes, agricultural or forest lands are taken by built-up areas to fulfill the demand of urbanization (Seto et al., 2012; Song et al., 2018); (ii) compared with urban growth as a single-dimensional change, **urban land use intensification**, also known as urban renewal, refers to a variety of integrated changes occurring in built-up areas, such as changes in its density (e.g., constructing and updating low-rise infrastructures into high-density ones) (Li et al., 2020a), changes in its uses (e.g., remodeling old built-up areas and buildings into new uses), and cleaning out urban slums (Mahta et al., 2019; Stokes and Seto, 2019); (iii) **deurbanization**, occurs whereby urban built-up areas are changed back to green fields for conservation, recreation or other purposes (Satterthwaite et al., 2010); (iv) **urban land use degradation**, changes urban areas into less developed areas, or sometimes into vacant lands (Long and Wu, 2016); and (v) **no change**.

#### 3.2. Time series modelling

Fitting time series model can isolate trend term from seasonality and noises incurred by abnormal signals, outliers and background noises (Gómez et al., 2016; Zhu et al., 2019). We proposed a non-linear

Logistic-Harmonic (LogH) model to fit monthly VIIRS time series (Eq. (1)), where the trend and seasonality of NTL were modelled by a logistic and two harmonic terms, respectively. The sigmoid function has been demonstrated for its superiority over linear model in quantifying different urban development stages and trajectory types, making it suitable for presenting the trend of NTL changes (Song, 2016). The harmonic terms were widely used to offset and to eliminate intra-annual seasonality of VIIRS data (Xie et al., 2019; Zhao et al., 2020a).

$$Y_{log}(t) = \frac{a}{1 + e^{bt+c}} + d + \sum_k^2 \left[ f_k \sin\left(\frac{2\pi kt}{12}\right) + g_k \cos\left(\frac{2\pi kt}{12}\right) \right] \quad (1)$$

where the estimated  $Y_{log}$  is a function of  $t$  (the  $t^{\text{th}}$  month of observation) with the following parameters:  $a$  (magnitude factor),  $b$  (change rate),  $c$  (timing of change),  $d$  (the initial background radiance value), and  $f_k$  and  $g_k$  (amplitude factors of seasonality);  $e$  is the base of natural logarithm. The number of harmonic term  $k$  is set to 2 to account for the annual and semi-annual seasonal variation based on our previous study with the Lomb Scargle Periodogram test (Zheng et al., 2019).

Model parameters of each VIIRS pixel time series were estimated by solving the non-linear least square model with the Levenberg-Marquardt algorithm. To ensure the quality of parameter estimation, two issues were taken into consideration: (1) Less representative observations. Subject to stray light and cloud coverage,  $cf_{cvg}$  value, an indicator of the representativeness of the observation of each month, differs substantially for each month. Ye et al. (2020) reported that less representative observations (i.e.,  $cf_{cvg}$  values were small or equaled to 0) occurred in 12% months of each VIIRS pixels. In this study, to reduce the impact of less representative observations on the model fitting, observations whose  $cf_{cvg}$  value was at the lower 12% of  $cv_{cvg}$  values were masked out. (2) Initial values of parameters estimation. Considering

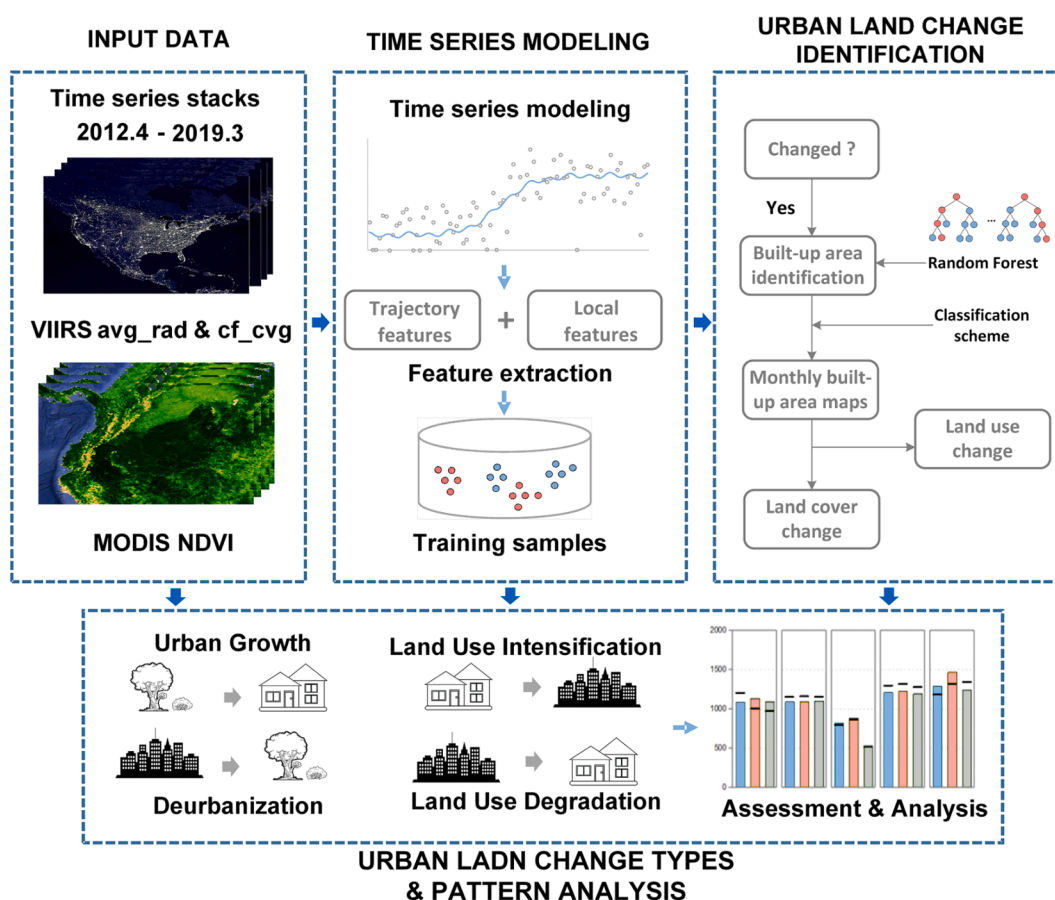


Fig. 2. Flowchart of the proposed analytical framework.

logistic curve is designed to fit trajectories in different patterns, it could be a full logistic curve (Fig. 3a) or only a portion of the entire curve (Fig. 3b). In the case of estimating parameters from partial logistic curves, the modelling performance is extremely sensitive to the input initial values. To cope with this issue, we initialized the fitting process with a heuristic initial guess of model parameters to ensure a satisfying fitting performance for any given type of time series trajectory (The initial parameter estimation and parameter sensitivity analysis can be found in Appendix A2).

This algorithm aims at providing a preliminary assessment whether a statistically significant change had occurred, and determining the most suitable time series model, either the proposed LogH model or the Linear-Harmonic model (LinH, see Appendix A2). Briefly, if a time series is not changed or has a higher  $R^2$  with LinH model, it is fitted by LinH model; otherwise, the time series is fitted by LogH model. Specifically, the modelling takes on five steps (see pseudo code of VIIRS time series fitting algorithm at Table A2).

- **Step 1:** remove low-quality observations;
- **Step 2:** linear regression is employed to determine whether a change occurs with statistical significance;
- **Step 3:** estimate initial values of parameters;
- **Step 4:** fit the time series data with LogH model;
- **Step 5:** avoid overfitting. Overfitting problem was observed when fitting low radiance time series with logistic model, especially for non-built-up pixels (Yang et al., 2017). A predefined change magnitude threshold ( $3 \text{ nW/cm}^2/\text{sr}$ ) is set to identify over-fitted pixels and to fit them with LinH model;
- **Step 6:** find the best fitting model. The best fitting model, either LinH or LogH, is determined by comparing the corresponding  $R^2$  value.

### 3.3. Urban land change characterization

#### 3.3.1. Trajectory and local features identification

The trajectory shape of the trend term may vary significantly during the study period, i.e., from  $t_1$  to  $t_{84}$ . It can be a full logistic curve (Fig. 4a), and a partial curve covering most part (Fig. 4b) or even only a small part (Fig. 4d) of the full curve. Using the estimated model parameters directly as input features would impair the classification accuracy (Gómez et al., 2016). The metrics and statistical features derived from time series trajectories are robust and stable (Vogelmann et al., 2016). In this study, the feature space was established with trajectory features from the estimated trend term and local features from the target

dates (Table 1). When VIIRS time series data was modelled by LinH model or less than one (included) of  $t_{cp1}$ ,  $t_{cp2}$  or  $t_{cp3}$  was within the study period ( $t_1$  to  $t_{84}$ ),  $t_{cp1}$ ,  $t_{cp2}$  and  $t_{cp3}$  was set as  $t_1$ ,  $t_{42}$  and  $t_{84}$ , respectively (Fig. 4d), to ensure the quality and robustness of the extracted features.

#### 3.3.2. Stable built-up and non-built-up samples selection

To generate monthly built-up area maps, a more ideal way was to collect monthly high-resolution training samples for the selected megacities. Limited by data availability and cost, it was barely possible to do so. Here, we employed an alternative approach to generate monthly built-up and non-built-up training samples. Our objective was to find unchanged built-up and non-built-up pixels throughout the study period using yearly MCD12Q1 land cover product, so that these stable pixels could be used for training. For each megacity, 500 built-up and 500 non-built-up pixels were randomly selected from MCD12Q1 as stable training samples. We employed some selection criteria to ensure the quality of stable samples (see Appendix A3 for details). The resulting valid stable samples and the corresponding features obtained from Section 3.3.1 were used to train the Random Forest (RF) classifier.

#### 3.3.3. Built-up areas classification

First, we proposed a new classification scheme to generate monthly built-up maps. We adopted a common definition to define urban built-up pixels based on impervious surface fraction ( $>20\%$ ) so that the urban built-up pixels defined here were consistent and comparable with most of previous studies (Xie and Weng, 2017). The rationale behind this scheme was that the VIIRS time series data was modelled as a whole process in this study. It is assumed that urban land changes are one-way processes, and that is unlikely to change back and forth constantly between built-up areas and non-built-up areas. The trajectories of NTL time series can provide hints for urban land change information, and thus we would not necessarily need to classify built-up areas for 84 times for the 84-month study period as the traditional month-by-month scheme would do. For an individual pixel time series, the proposed classification scheme assumes that:

- The land cover types, i.e., built-up or non-built-up, of all the months during pre-change stage,  $t_{pre\_change} = [t_1, \dots, t_{cp1}]$ , remain the same. Similarly, the land cover types are the same for the months during post-change stage,  $t_{post\_change} = [t_{cp3}, \dots, t_{84}]$ . Thus, it is not necessary to implement classification for each month of pre-change or post-change stages. Instead, we only need to know the land cover type of a certain month during pre-change (or post-change stage) so that

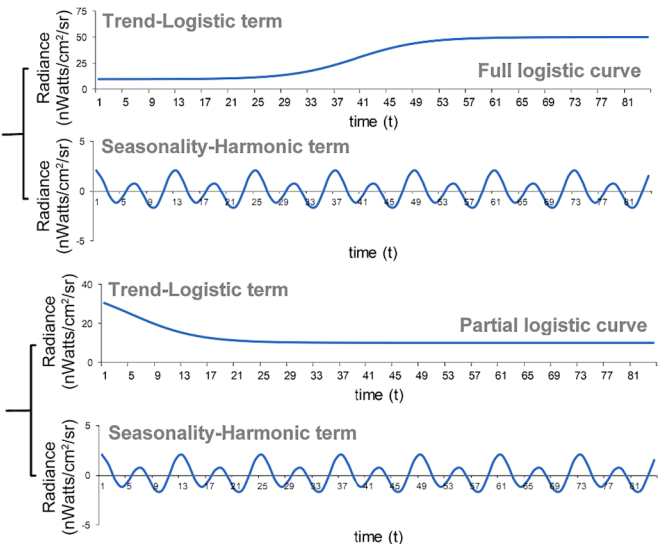
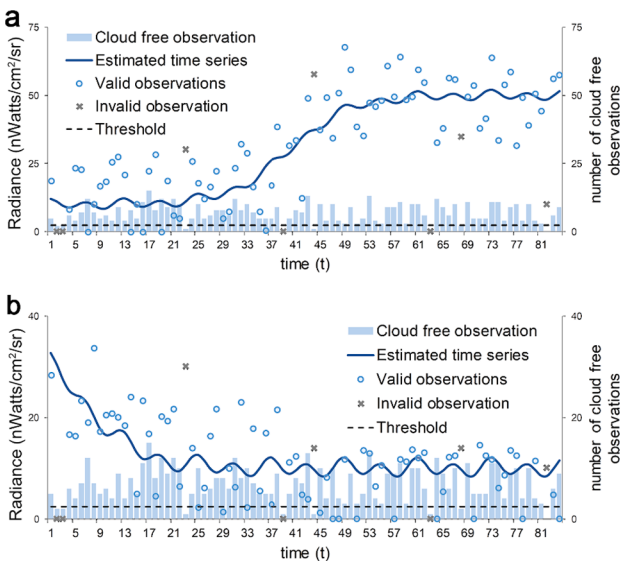
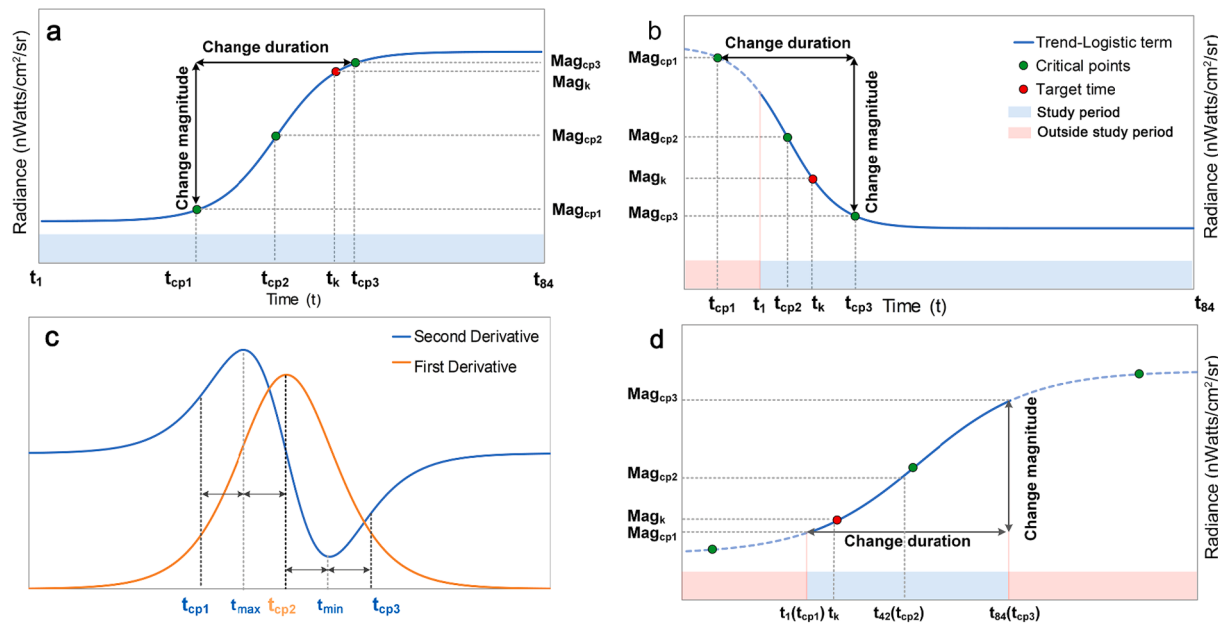


Fig. 3. LogH model fitting: full logistic curve (a) and partial logistic curve (b).



**Fig. 4.** An illustrative diagram of NTL trajectory and local feature extraction. Full logistic term (a), and its first and second derivative (c); partial logistic curve (b) and (d). In the case of (d), adjustments are made in terms of how to extract features.

**Table 1**  
Explanation of trajectory and local features.

Trajectory features	
Critical points 1 (CP1)	The start of change, $t_{cp1} = 2t_{max} - t_{cp2}$
Critical points 2 (CP2)	The point with largest change rate, $t_{cp2}$
Critical points 3 (CP3)	The end of change, $t_{cp3} = 2t_{min} + t_{cp2}$
NTL radiance of CPs	$Mag_{cp1}, Mag_{cp2}, Mag_{cp3}$
Change magnitude	$Change_{magnitude} = Mag_{cp3} - Mag_{cp1}$
Change duration	$Change_{duration} =  t_{cp3} - t_{cp1} $
Change rate	$Change_{rate} = Change_{magnitude} / Change_{duration}$
Seasonality magnitude	$Seasonality_{magnitude} = \sum_k \sqrt{f_k^2 + g_k^2}$ ( $f_k$ and $g_k$ are the amplitude factors of seasonality)
Local features	
Time of target date	$t_k$
NTL radiance of target month	$Mag_k$
Maximum NDVI (MOD13A1)	NDVI <sub>max</sub> is the maximum NDVI value within the 12 closest months of the target month ( $t_k$ ). For example, if the target month is Jan 2015, the NDVI <sub>max</sub> is determined by the maximum NDVI value between July 2014 and June 2015.

the land cover types of all months during the pre-change ( $LC_{pre\_change}$ ) (or the post-change stage,  $LC_{post\_change}$ ) can be determined.

- If the months of pre-change and the post-change stages belong to the same land cover type, it indicates that the urban land cover type has not been changed from  $t_1$  to  $t_{84}$  (Table A2 (a) and Fig. 5a). Only when the land cover type of pre-change stage differs from that of post-change stage, it is necessary to carry out further classification for the months of changing stage,  $t_{changing} = [t_{cp1+1}, \dots, t_{cp3-1}]$  (Table A3(b) and Fig. 5b).

Based on the above consideration, our proposed classification scheme is as follows:

- Step 1:** For each VIIRS pixel time series,  $t_{cp1}$  and  $t_{cp3}$  are assigned as the target dates and implemented a RF classification using the trajectory and local features derived in Section 3.3.1 to determine land cover type of the entire pre-change ( $LC_{pre\_change}$ ) and post-change

stage ( $LC_{post\_change}$ ), respectively. In order to avoid misclassification an additional RF classification is applied to  $t_{cp2}$  as a double check operation. Our sensitivity analysis indicated that selecting  $t_{cp1}$  (or  $t_{cp3}$ ) or other dates in pre-change (or post-change) stage to determine  $LC_{pre\_change}$  (or  $LC_{post\_change}$ ) was insignificantly ( $P < 0.001$ ) correlated with the classification accuracy (refer to Appendix A3 for further details).

- Step 2:** If  $LC_{tcp1} = LC_{tcp2} = LC_{tcp3}$ , it suggests that  $LC_{tcp1}$  and  $LC_{tcp3}$  are accurately classified and no land cover change has occurred during the study period (Table A3 (a) and Fig. 5a). If  $LC_{tcp1} = LC_{tcp3}$  but  $LC_{tcp1} \neq LC_{tcp2}$  or  $LC_{tcp2} \neq LC_{tcp3}$ , it implies that either  $LC_{tcp1}$  or  $LC_{tcp3}$  is misclassified (Table A3 (b)). If  $LC_{tcp1} \neq LC_{tcp3}$ , it indicates the occurrence of land cover change during the study period.
- Step 3:** RF classification is implemented from  $t_{cp1}$  to  $t_{cp3}$  at a 1-month interval until three consecutive months are found, where  $LC_{tk} = LC_{tk+1} = LC_{tk+2}$  but  $LC_{tk-1} \neq LC_{tk}$  (Table A3 (c) and Fig. 5b). Land cover types for  $t_1 - t_{k-1}$  and  $t_k - t_{84}$  are set as  $LC_{tk-1}$  and  $LC_{tk}$ , respectively.

The built-up mapping accuracy was assessed from three aspects: First, we generated two ground truth reference datasets to evaluate the resulting built-up maps on a pixel basis. (1) Visually interpreted from the ground truth data: We randomly selected and visually interpreted 50 built-up (impervious surface fraction  $> 20\%$ ) and 50 non-built-up ground truth pixels for each megacity (i.e., 1500 built-up and 1500 non-built-up pixels in total) with the help of Landsat images and Google Earth historical images. Specifically, for a certain pixel, we identified cloud-free Landsat or available Google Earth historical images and then visually checked whether the pixel in the corresponding month was accurately classified. (2) GHSLviirs ground truth: We utilized GHSL, a medium spatial resolution built-up map product in 2014 (Pesaresi et al., 2013), to generate another ground truth data (GHSLviirs) for a joint assessment. If a 500-m VIIRS grid (GHSL<sub>viirs</sub>) contained  $> 20\%$  of built-up areas derived from GHSL, it was labelled as a built-up pixel. GHSL<sub>viirs</sub> was then used to validate the resulted built-up map of each megacity in December 2014. Second, we compared the built-up area extent in December 2014 with that from MCD12Q1 and GHSL in 2014. Third, to further assess the effectiveness of our method, additional comparisons were implemented as follows: (1) Excluding NDVI as the input feature

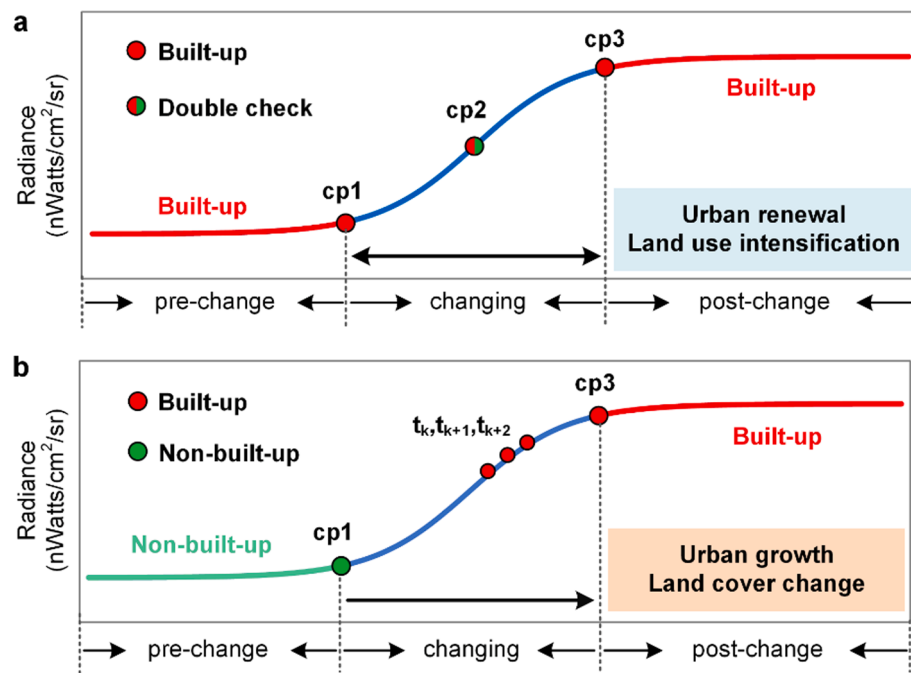


**Fig. 5.** Illustration of the proposed classification scheme for two types of urban land change: (a) urban land use intensification (urban renewal); and (b) urban growth (land cover change).

(Model 2 in Table 3); (2) Incorporating temporal information and month-by-month classification scheme, rather than the proposed classification scheme (Model 3 in Table 3). This comparison was to separate the contribution of temporal information from the proposed classification scheme on mapping accuracy improvement; (3) We obtained the monthly built-up maps with three widely-adopted spectral-based methods, including thresholding method using raw VIIRS data (Liu et al., 2012) or a NTL index—VANUI (Zhang et al., 2013), and classification-based method (Dou et al., 2017) (Model 4–6 in Table 3).

### 3.3.4. Urban land change types identification

Based on the monthly built-up area maps and the trend of NTL change, we disentangled urban land change of each pixel into the following five types (Table 2). The urban land change type of a built-up pixel was labelled as land use change when (1) the NTL intensity was changed with statistical significance (Section 3.2) but (2) land cover change did not occur in this pixel. We further used the trend of NTL change, either increasing or decreasing, to indicate urban land use intensification or degradation.

## 4. Results

### 4.1. Time series modelling

Fig. 6 summarizes the fitting performance for all pixels time series of

**Table 2**  
Urban land change types identification.

Pre-change stage	Post-change stage	Urban land change types
Built-up	Built-up (NTL increasing)	Land use intensification (Urban renewal)
Non-built-up	Built-up	Urban growth (Land cover change)
Built-up	Non-built-up	Deurbanization (Land cover change)
Built-up	Built-up (NTL decreasing)	Land use degradation
Non-built-up	Non-built-up	No LULC change
No significant change in NTL		No LULC change

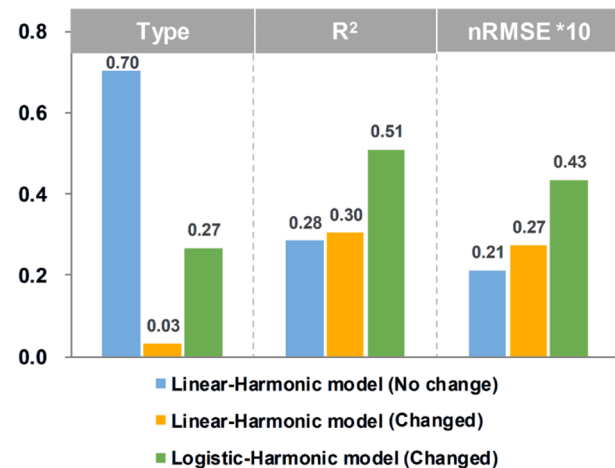


**Fig. 6.** Results of time series modelling. nRMSE is multiplied by 10 for a better illustration.

the 30 megacities. It shows: (1) the ratio of pixels fitted by LinH model and the LogH model, and pixels that do not change in statistical significance (No change); (2) mean R<sup>2</sup> values; and (3) mean normalized RMSE (nRMSE ∈ [0,1]). Among the changed time series, nearly 90% were fitted by the LogH model, which showed a better fitting performance ( $R^2 = 0.51$ ) than the LinH model ( $R^2 = 0.30$ ). The mean  $R^2$  of LogH model ranged from 0.34 (Vancouver) to 0.66 (Delhi) over 33 megacities (see Table A4). The mean nRMSE was around 0–0.1 for all cities. The LogH model exhibited a slightly higher mean value of nRMSE (0.043) than that of the LinH model (0.027). This was because the time series fitted by the LogH model had a higher data variation than those by the LinH model.

It was found that the proposed LogH model was effective in characterizing a great variety of VIIRS trajectory patterns. Fig. 7 presents the fitting performance of eight typical trajectories of VIIRS time series. These trajectories are different in term of their trend (increasing or decreasing), type of change (gradual or abrupt), and the shape of logistic

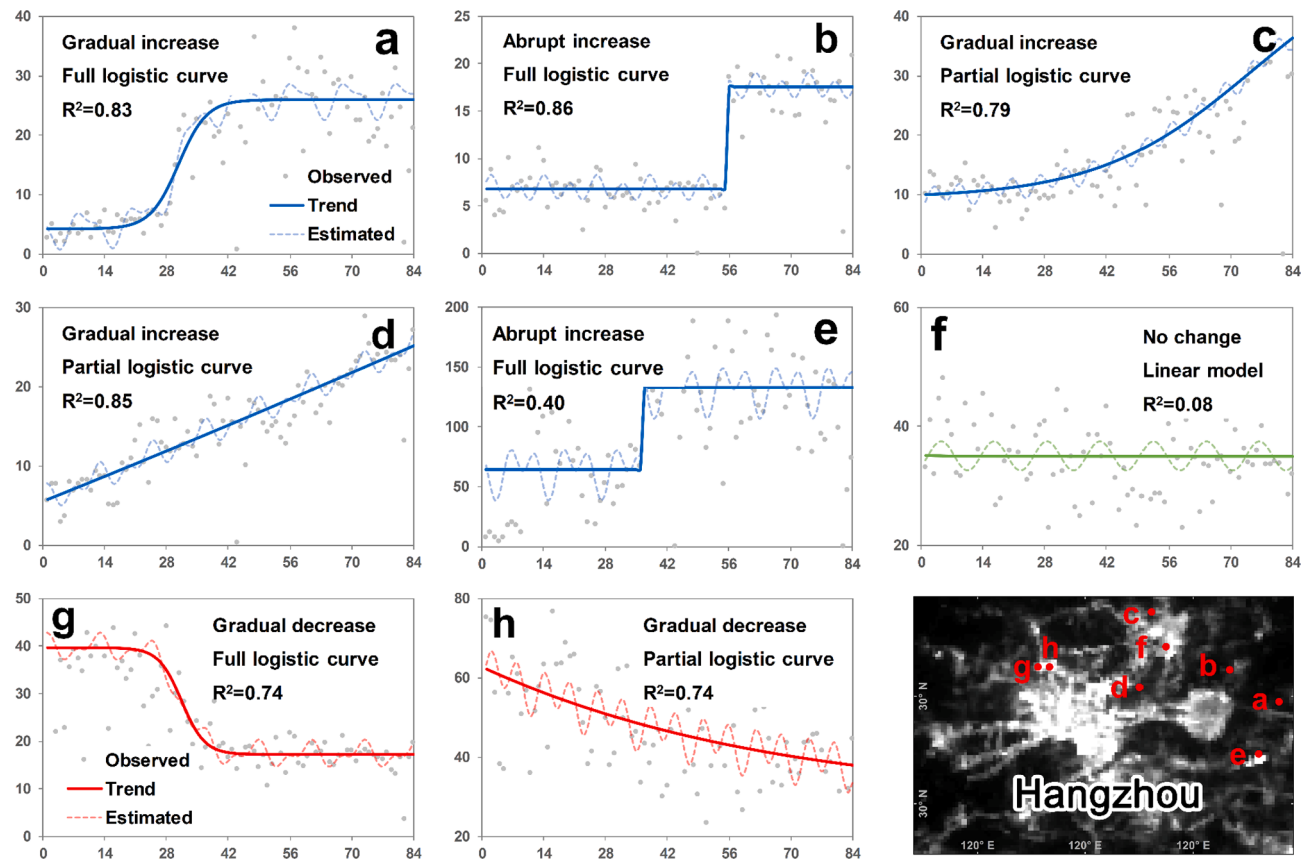


**Fig. 7.** Eight typical trajectories of the VIIRS time series in Hangzhou, China. X-axis: the  $t^{\text{th}}$  month of observation; y-axis: VIIRS radiance ( $\text{nW}/\text{cm}^2/\text{sr}$ ). (a) - (e) and (g) - (h) are modelled by LogH model. (f) is a pixel that is not significantly change and thus is fitted by LinH model.

curve (a full curve or a partial curve). The fitting performance was largely secured by the initial parameter estimation. Without initial parameter estimation, the mean  $R^2$  value would drop sharply from 0.51 to 0.13, and the LogH model would fail in fitting most of the partial logistic curves, as shown in Fig. 7c, 7d and 7 h. The difficulties in modelling the seasonal effect of VIIRS time series was the main reason of a moderate  $R^2$  value (0.51). Many issues about the seasonality of VIIRS remained unclear (Levin, 2017; Xie et al., 2019). Even with some degree of overestimation and underestimation in modelling the seasonal changes, the LogH model was still able to capture the changing trend of the time series, which was the key determinant of urban land change type identification. Taking an extreme case as an example, Fig. 7e displays a pixel located at an International Airport. The artificial light emission therein was distinct from other urban areas, where the seasonal effect of time series exhibited an exceptionally larger variation. A further inspection revealed that the modelling performance ( $R^2$ ) was not related to the latitude of a megacity ( $P < 0.01$ ). It implies that the proposed model was robust to data quality variation, resulted from stray light at high latitudes and frequent cloud coverage at low latitudes.

#### 4.2. Urban built-up area mapping

A linear regression analysis was conducted to compare results of built-up areas mapping obtained from the proposed method, MODIS-based MCD12Q1 and Landsat-based GHSL (Fig. 8). A high consistency was found to exist between our result and MCD12Q1 ( $R^2 = 0.98$ ) and a slightly lower agreement with GHSL ( $R^2 = 0.89$ ). The major inconsistencies were embodied in the scattered and low-density human settlements at urban outskirts and intercity highways.

Table 3 compares the built-up area mapping accuracy of the proposed method (Model 1) with two testing methods (Model 2–3) and

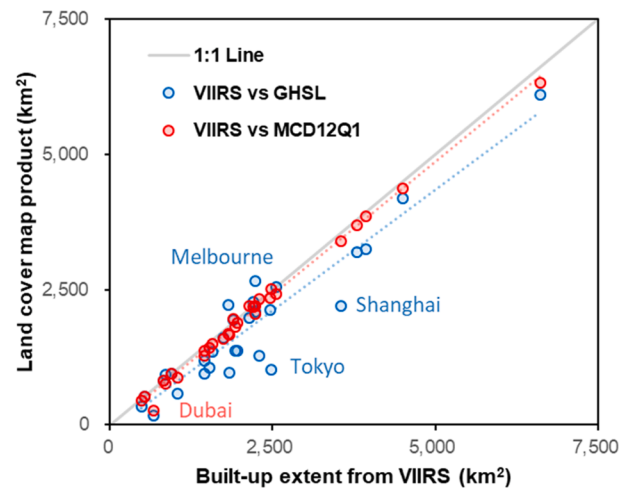


**Fig. 8.** A comparison between built-up areas obtained from NTL data (December 2014) and land cover product (MCD12Q1 and GHSL<sub>VIIRS</sub> in 2014).

three widely-adopted NTL-based built-up mapping methods (Model 4–6). Temporal features based methods (Model 1–3) generally yielded a higher overall accuracy, with an improvement up to 19%, than spectral-based methods (Model 4–6). By incorporating temporal features and the proposed classification scheme, our method (Model 1) showed the highest accuracy of 95% (against the visually interpreted reference data (VI), hereafter), and 91% (against the GHSL data, hereafter). At the city level, the mapping accuracy varied from 90% (VI) or 86% (GHSL) in Guangzhou, China to 96% (VI) or 92% (GHSL) of Sao Paolo, Brazil. The

**Table 3**  
Accuracy assessment of the different models.

Model	Type	Type	Feature sets	Ground Truth Reference	
				VI	GHSL <sub>viirs</sub>
1	Classification*	Temporal	Temporal features; NDVI	95.3%	90.6%
2	Classification*	Temporal	Temporal features	94.0%	89.4%
3	Classification	Temporal	Temporal features; NDVI	86.7%	86.9%
4	Thresholding	Spectral	VIIRS	75.6%	71.1%
5	Thresholding	Spectral	VANUI (VIIRS + NDVI)	77.3%	79.1%
6	Classification	Spectral	VIIRS; NDVI	81.9%	82.4%

**Note:** Visually interpreted ground truth data (VI) was used to access the accuracy of the selected validation samples of the corresponding month when Landsat and Google Earth historical images are available; GHSL<sub>viirs</sub> was used to evaluate the accuracy of the built-up area map in December 2014 only. Model 1 is the proposed method. Please refer to Section 3.3.3 for detailed description of the comparative models (Model 2–6). \* indicates the monthly built-up maps are generated by the proposed classification scheme, while others are derived by traditional month-by-month classification scheme. Please refer to Table A5 for the producer's and user's accuracy.

high classification accuracy was ascribed to two factors: incorporating temporal information and implementing the proposed classification scheme. Comparing Model 1 and Model 3, it was found that the accuracy improvement against the selected traditional methods (Model 4–6) was mainly resulted from incorporating temporal information, while using the proposed classification scheme further increased the built-up mapping accuracy by 8.6% (VI) and 3.7% (GHSL).

Fig. 9 presents a detailed comparison of built-up areas identified by our method (Model 1), thresholding method with NTL index—VANUI (Model 4) and spectral feature based classification method (Model 6). It shows a clear advantage of the proposed temporal feature based method in dealing with heterogeneous landscapes. For cities with high amount of built-up pixels, e.g., Shanghai (Fig. 9c) and Melbourne (Fig. 9f), Model 1 produced an accuracy 6–13% (VI) higher than that of Model 4 and Model 6, respectively (Table 3). The accuracy improvement was more prominent for cities with a highly heterogeneous built-up/non-built-up landscape, where the overall accuracy of Model 1 surpassed Model 4 and Model 6 by 10–22% (VI), respectively, e.g., Hangzhou (Fig. 9a) and Bangkok (Fig. 9d). This merit appeared at both urban outskirts and inner-city areas. In the case of inner-city areas, for example, Site 1 of Fig. 9b was located in the Central Ridge Forest Reserve of the downtown Delhi, India. The forest reserve was surrounded by a number of commercial buildings and public infrastructures, as well as scenic spots. It has been reported that urban green spaces that are scenic spots or close to commercial areas tend to be brightly lit, sometimes even brighter than built-up areas (Zheng et al., 2018). For this case, the light emitted from roads and scattered by adjacent infrastructures combined to render a medium-level NTL intensity (18 nW/cm<sup>2</sup>/sr) to the forest area. Both Model 4 and Model 6, based on the spectral features of NTL and NDVI, could not differentiate the forest reserve from the surrounding built-up areas. In contrast, by using temporal feature alone (Model 2) or combining temporal feature with NDVI (Model 1), a major part of forest reserve (67%) could then be identified as non-built-up areas. Misclassification occurred at the northern part of the forest due to the bright light from traffic and buildings therein and light diffused from the adjacent commercial areas (Sanchez de Miguel et al., 2020). In addition, urban green roofs may be another potential factor leading to misclassification in urban centers. This finding suggests that albeit a noticeable improvement against traditional methods, we could not fully eliminate misclassification in inner-city areas, especially for urban green spaces adjacent to populous areas. In another example, Model 1 showed a considerably higher accuracy than other models in mapping built-up areas at the outskirt

regions of Chicago, USA, where residential houses were mixed with cropland and bare land (Site 2 of Fig. 9e).

#### 4.3. Urban land change type identification and analysis

Our classification scheme generated urban built-up area maps for 84 months with temporal consistency (red line in Fig. 10). By contrast, although Model 6 showed the best classification result among spectral-based methods, the classification error showed a highly fluctuated built-up/non-built-up area time series (black dash lines in Fig. 10). This problem was deteriorated when LULC change occurred in the time series, such as site 1 of Fig. 10a–10c.

Based on the monthly built-up areas maps, we identified urban land change types for each pixel and disentangled them into five categories, including: (1) no change (NC); (2) urban growth (UG); (3) urban land use intensification (NTL increase, LUI); (4) urban land use degradation (NTL decrease, LUD); (5) deurbanization (DU). Fig. 10 provides examples of these five categories, including: gradual urban growth (Fig. 10a site 1, Chengdu); rapid urban growth (Fig. 10c site 1, Cape Town); urban land use intensification (Fig. 10a site 2, Chengdu) from factory to high-rise commercial complex; urban land use degradation from construction site to abandoned field (Fig. 10d site 1, Sao Paolo); deurbanization (Fig. 10b site 1, Beijing) where old-style human settlements are cleared out for a city park; and no significant LULC change (Fig. 10c site 2, Cape Town) where the site remained as bare land.

We then analyzed the pattern of urban land change types of 30 megacities (Fig. 11). As a whole, statistically significant changes were found in over 52% of urban built-up pixels (excluding non-built-up pixels). This proportion, however, varied greatly with megacities, from Berlin (11%) to Buenos Aires (59%) and Jakarta (89%). One noteworthy finding was that together, urban land use intensification (83%) and degradation (13%), accounted for an overwhelming proportion (96%) of urban changes, whereas urban growth only accounted for 3%. To analyze the spatial variation of different urban land changes, we identified the urban center using Xiao et al. (2014) and used a buffer analysis approach to divide urban built-up area into urban core and urban outskirt with an equal spatial extent. It was found that urban growth, deurbanization, and urban land use degradation mainly occurred in urban outskirts while urban land use intensification and no change were distributed evenly over entire city.

However, a considerable contrast in urban change patterns was observed between megacities in developed countries and those in developing countries (Fig. 12). First, the pixels of megacities in developing countries (50%) were more likely to have a logistic urban development trajectory than those in developed countries (30%). Second, a greater extent of urban land change was observed in megacities of developing countries (58% of the pixels) than those of developed countries (40%) (Fig. 12). In developing countries, coastal megacities in Southeast Asia and Africa appeared to be hotspots of urban land changes, such as Jakarta (89%), Nairobi (87%) and Kuala Lumpur (77%). Third, the megacities in developing countries underwent a significantly higher proportion (60%) of urban land use change, in both intensification and degradation, than those in developed countries (18%). In light of urban land use change magnitude, the megacities of developing countries exhibited a higher magnitude of land use intensification (5.2 nW/cm<sup>2</sup>/sr) but a lower magnitude of land use degradation (-7.0 nW/cm<sup>2</sup>/sr) than those of developed countries, with the magnitude of 3.2 nW/cm<sup>2</sup>/sr and -8.2 nW/cm<sup>2</sup>/sr, respectively. In spite of a relatively low average urban land change percentage, some megacities of developed countries showed a surprisingly high urban land change percentage, especially land use change, such as Tokyo (57%) and Rome (85%). This phenomenon could be ascribed to the growth of high-rise buildings and increased land use intensity, which is evoked by the high land prices and the limited space for horizontally outward urban growth in well-developed cities (Mahtta et al., 2019).

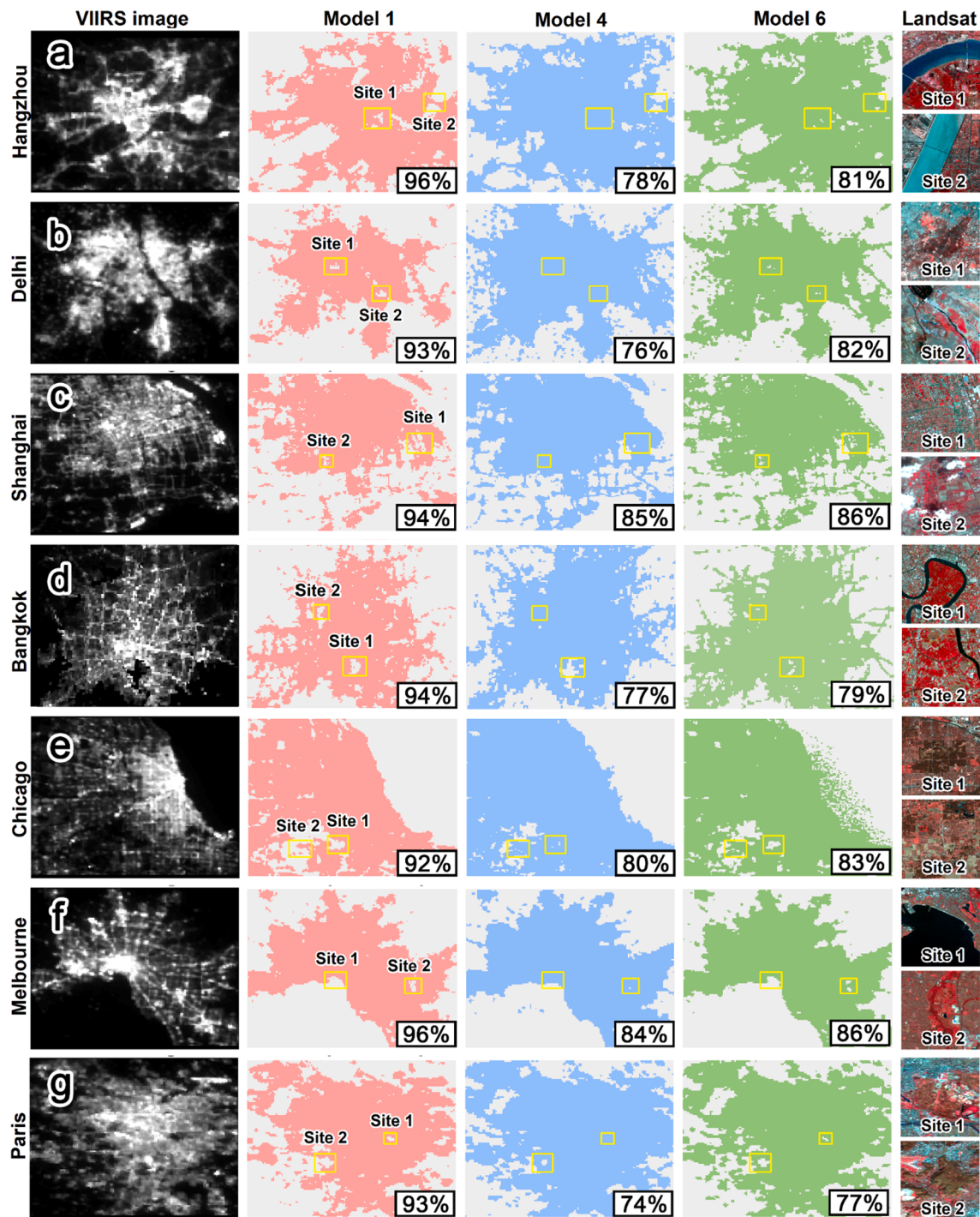


**Fig. 9.** The left panel is VIIRS image; the middle panel is built-up areas derived by three different methods (Table 3) with accuracy being indicated; the right panel include zoomed-in Landsat images. The accuracy values were based on the ground truth reference generated by visual interpretation. Please refer to Table 3 and Selection 3.3.3 for further details.

## 5. Discussions

### 5.1. Urban built-up area mapping

In this study, temporal features derived from monthly VIIRS time series were used to generate monthly urban built-up areas maps. Compared with traditional spectral-based methods, the advantages of the proposed method lied in the following aspects. First, spectral-based thresholding and classification methods depend only on the spectral value of a pixel, so they cannot effectively distinguish non-built-up areas

with moderate or high NTL values from built-up areas, such as Site 1 in Fig. 9b. On the contrary, the NTL trajectories of built-up and non-built-up areas could vary significantly and thus are beneficial to differentiate them (Gómez et al., 2016; Zhu, 2017). This explains the high mapping accuracy of our method in non-built-up areas around urban outskirts and inside urban areas, where moderate and extremely high NTL value pixels exist (Fig. 9). Second, fitting time series model allows to isolate “noises” in the VIIRS time series, e.g., the seasonal effect and ephemeral signals, so that the temporal pattern can be better modelled. Third, the use of dense monthly VIIRS time series can track gradual changes as well

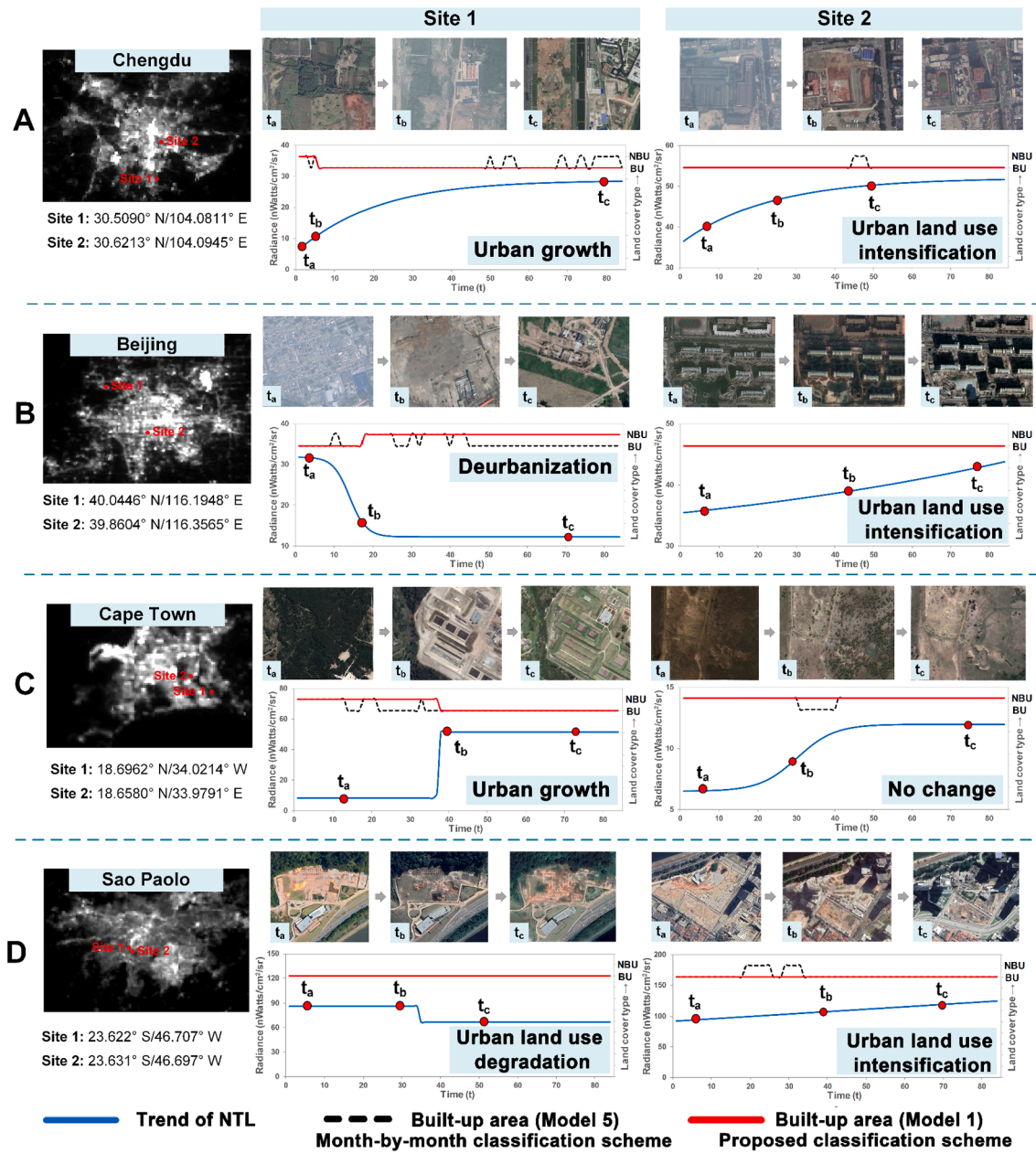


Fig. 10. Changes in urban built-up areas and the identified urban change types (refer to Table 2). BU: Built-up area; NBU: Non-built-up area.

as subtle and abrupt changes. These changes, as shown in Fig. 7b&7e, would be buried in annual NTL time series or land cover map products that are released at an annual or 5–10 years interval and with a lag of 1–2 years, such as GlobeLand30, GHSL and Global Urban Footprint (Esch et al., 2017; Pesaresi et al., 2013).

## 5.2. Mapping urban land change as a whole process

We developed a Logistic-Harmonic (LogH) model to fit monthly VIIRS time series. It is distinctly different from the Linear-Harmonic (LinH) model in terms of how urban land changes are modeled. The Linear or LinH models, such as BFAST (Verbesselt et al., 2010), CCDC (Zhu and Woodcock, 2014) and LandTrendr (Kennedy et al., 2010), divides land changes into a number of linear segments. In contrast, the proposed LogH model characterizes urban land change as a whole process. For the LinH models, a statistic boundary (threshold) is used to determine the occurrence of changes and to separate time series into segments. The effectiveness of fitting and the subsequent classification

thereby heavily rely on the appropriateness of threshold setting. When modelling a time series data as a whole process, the difficulty in thresholding can be avoided. In addition, LinH model treats each segment individually so only temporal features from a single segment are used for classification. Modelling time series as a process enables using information from the entire time sequence. Modelling the whole temporal process can leverage the unique characteristics of urban land changes. By doing so, our classification scheme leaves out unnecessary classifications and thus reduces classification errors and their propagation. Compared with traditional image-by-image classification scheme, our method improved the accuracy and temporal consistency. It was also found that the proposed classification scheme could remarkably enhance the classification efficiency. If the traditional image-by-image classification scheme was adopted, we could need to implement the classification for 84 times to produce 84 maps. In contrast, by using the proposed classification scheme, only 8.96 times of classifications on average were required to create 84 maps for 99.5% pixels of each megacity (Fig. 13).

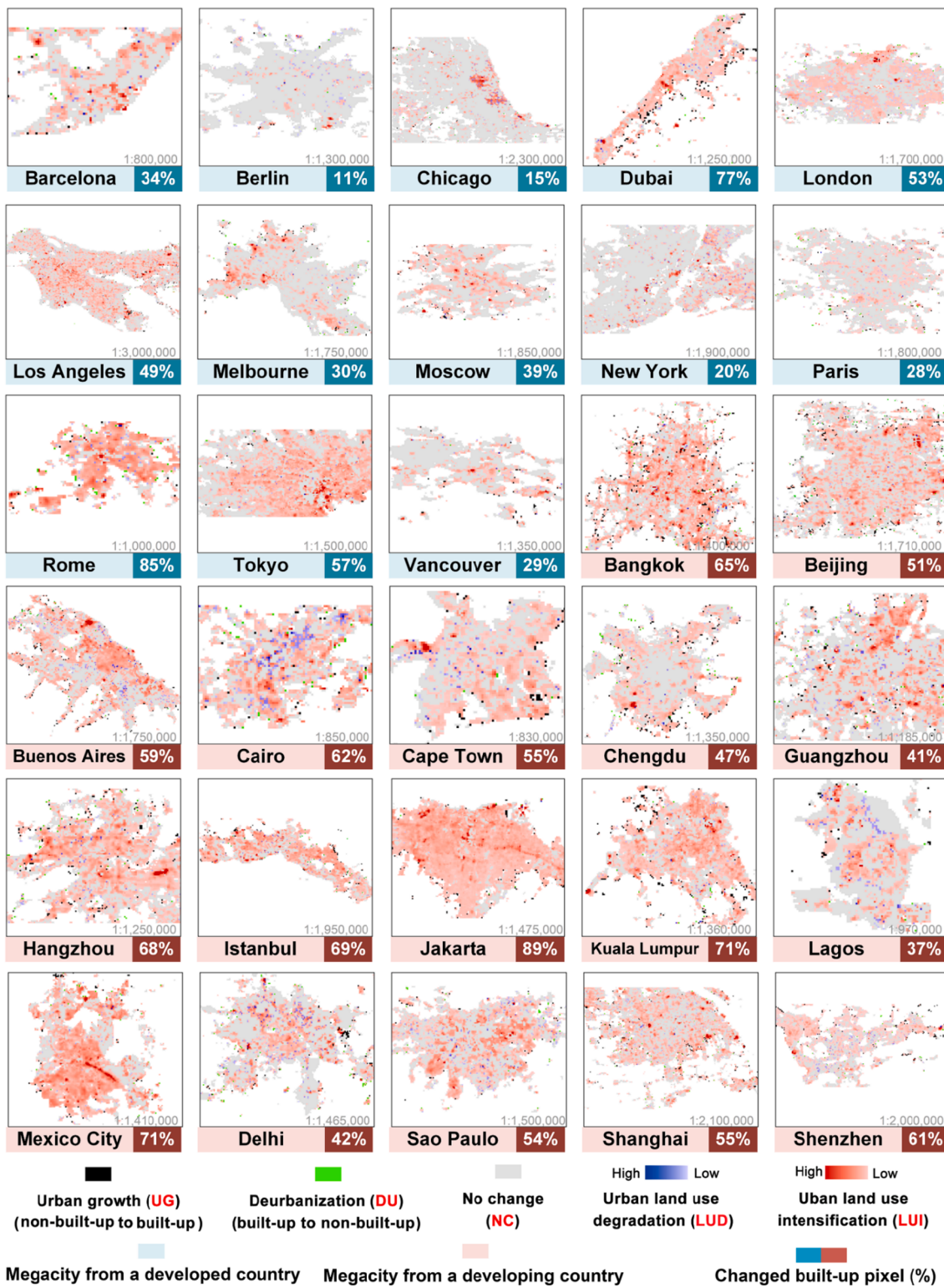
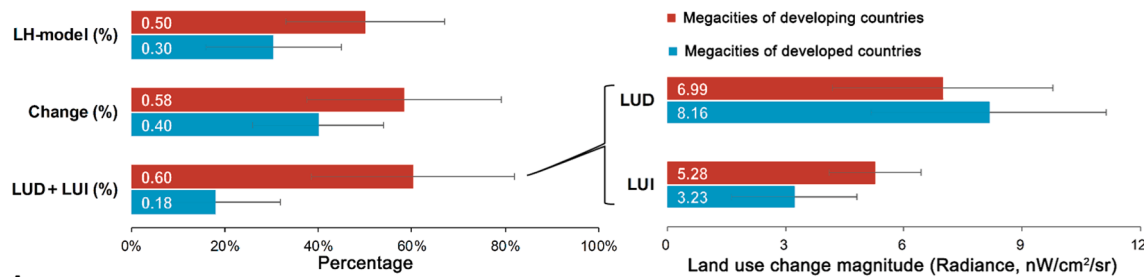


Fig. 11. Urban land changes in the 30 megacities. The percentage indicates the proportion of changed pixels in urban built-up areas.

### 5.3. The uniqueness of nighttime light image data

Existing time series methods like CCDC, BFAST and LandTrendr have been proven effective in detecting changes in forest disturbance and recovery, most land cover changes, and vegetation dynamics with reflectance, NDVI and NBR as input data. Nevertheless, our study has demonstrated that a new model is warranted to estimate urban land changes with nighttime light data due to its uniqueness. The reflectance

data, NDVI and spectral indices mainly reflect the physical properties of the Earth surface, i.e., land cover (Zhu, 2017), while NTL data records the light emission from urban infrastructures as an indication of both biophysical properties (land cover) and human activities (related to manner and purpose in which the land is used) in urban areas (Zhao et al., 2018). Therefore, the trajectories of NTL time series differs greatly from time series of reflectance and NDVI in the urban areas. As demonstrated in this study, the trend of NTL time series shows a non-



**Fig. 12.** Comparison of urban land characteristics of megacities. The colored bars and white values represent the average value, while the error bar represents the standard deviation for all megacities. LogH model (%): percentage of built-up pixels fitted by LogH model; Change (%): percentage of changed built-up pixels; LUD + LUI (%): percentage of built-up pixels with land use changes, including land use degradation (LUD) and land use intensification (LUI); The magnitude of LUD and LUI are shown in absolute values in the right panel.

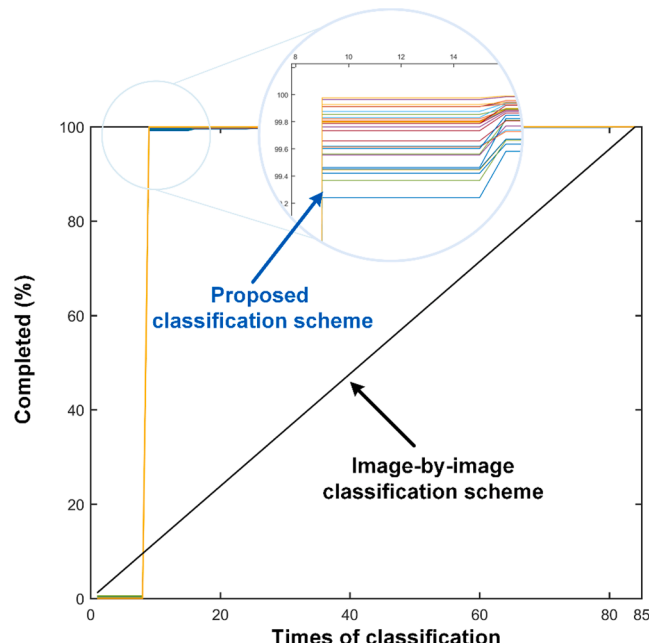


**Fig. 13.** Classification efficiency comparison between the proposed classification scheme of 30 selected megacities (colored lines) and month-by-month scheme (black line). The x-axis indicates the number (how many times) of classification has been implemented while y-axis presents how much percentage of pixels of a certain megacity has finished the classification for the entire study period ( $t_1-t_{84}$ ).

linear fashion and largely a gradual change process with an average change duration of  $35 \pm 8$  months for all megacities. This is because the spatial resolution of nighttime light data is coarse. The NTL change of a single light source, i.e., light's on-and-off, is an abrupt process. However, if we consider all light sources inside a 500-m VIIRS pixel, NTL change of the pixel would most likely be a gradual and non-linear pattern. For characterizing urban land changes with NTL data, the proposed time series model is thus more suitable than the models of CCDC, BFAST and LandTrendr.

NTL data encapsulates the merit of “daytime” remote sensing imagery in presenting land cover change as well as the particularity of geo big-data in revealing urban land use types. The vast majority of studies based on “daytime” remote sensing data can mainly map land cover changes. As revealed by our results, land use changes accounted for 96% of the urban land changes in the 30 megacities as compared with 4% of the land cover changes. Measuring urbanization with “daytime” remote sensing imagery cannot sufficiently reveal the complexity of urban LULC changes (Stokes and Seto, 2019). In stark contrast, NTL radiance/DN presents a holistic indication of human activities and land use intensity,

and is thus more suitable for this purpose (Kuechly et al., 2012; Levin, 2017; Zheng et al., 2020).

#### 5.4. Urban land use intensification vs. Urban growth

This study offers important information about how urban land changes over time, including urban land change types and their spatial extent, intensity and trend trajectory. These information brings tangible benefits to achieving the goals of sustainable urban development (Griggs et al., 2013; Seto et al., 2017). Two pertinent implications of our results are discussed below. First, land cover change, i.e., urban growth, attracts an overwhelming attention of previous urban studies with remote sensing technology. In contrast, remote sensing of land use changes and its environmental consequences needs more in-depth analyses, especially for how urban land use has been changed. Our results with NTL data demonstrate that land use intensification has been the major feature of urban land changes (83%) in the megacities. This finding implies that the trend of urbanization might have gradually shifted to land use intensification for global megacities, which corroborates with results of some previous studies (Li et al., 2020b; Mahtta et al., 2019). It also prompts the necessity of understanding the consequences of such dramatic land use intensification at global scale, such as how it affected the urban environment and local climate, reshaped urban energy use, and changed urban population distribution. Additionally, a distinct pattern of urban land change was observed between megacities from developing countries and those from developed countries. This difference provides compelling knowledge with regard to urban spatial planning, especially in developing countries. Lessons from developed countries in urban land trajectories offers a reference for developing countries and cities which are undergoing rapid urbanization.

#### 6. Limitations

There are a few limitations in our proposed method. First of all, within a VIIRS pixel, land cover change (e.g., urban growth) and land use change (e.g., urban land use intensification) might occur at the same time. Precisely speaking, the urban land change type we refer to in this study is actually the dominant type of change within a pixel. The mixed pixel issue is a prevailing problem for coarse resolution images, including VIIRS images (Zhu et al., 2019). We did not cope this issue because the relationship between NTL intensity and urban land use types is unclear and also varies greatly in different regions (Kuechly et al., 2012; Zheng et al., 2018).

Two issues about the time series modelling are worthy of further discussion and improvements. First, the assumption behind our proposed method was that there was only one dominant urban change type during the study period. In some cases, two consecutive urban land changes might occur, e.g., urban growth followed by urban land use intensification. This would give rise to a problem in the time series modelling, as well as subsequent urban land change characterization.

However, our assessment with 2000 randomly selected built-up pixels time series showed that multi-stage urbanization rarely occurred (<0.1%). This was probably because the study period was relatively short (7 years) due to the availability of monthly VIIRS data. Previous long-term studies spanning over 20 years, such as Xu et al. (2014) and Song (2016), also supported our argument that multi-stage urbanization was not prevailing. Second, special events, such as regional armed conflicts, natural disasters and pandemics (e.g., COVID-19), could result in unexpected disturbance in the VIIRS time series. For example, the detected radiance would drop and then slowly recover due to power outage after a hurricane (Román et al., 2019), which might be misidentified as land use degradation. Nevertheless, the 30 selected megacities in this study were relatively stable and were not observed with influential events during the study period, from April 2012 to March 2019. Moreover, short-term events, e.g., power outage for a day or two, will have little impact on urban land change identification. This is because the VIIRS data used in this study is a monthly averaged composite data, so a temporary decrease would not likely to cause significant radiance change in the corresponding month, not to mention the entire study period.

The transition in lighting facilities is another potential factor. Urban land use intensification as detected by nighttime lights, may not necessarily reflect a transition from ground level houses to high-rise buildings. It may also result from the installation of better lighting in the city, without any material changes in the buildings. The spectrum of VIIRS ranges from 500 nm to 900 nm. As a result, a certain proportion of light in the blue part of the spectrum cannot be detected, such as the light emitted by white LED lamps (Zheng et al., 2018). Thus, transition to LED lighting would potentially cause of NTL radiance decrease (Levin et al., 2020), which consequently may influence urban land change identification. Even so, the mechanism of how the transition in lighting facilities affects the detected NTL radiance is still less clear under large spatial settings. To further probe into this issue, multispectral sensors, or at least panchromatic sensors that include the blue spectrum, are imperative. Adding urban building height information, as it is a more direct indicator of urban land use intensification, is solution to exclude the influence from lighting facility transition.

The overpass time of VIIRS is around 1:30 am, which will lead to a decrease in the detected light and thus will have a potential impact on urban land change identification. We argue that in spite of a less ideal overpass time of VIIRS data, there is still plenty of lighting to be detected by VIIRS, even after midnight (Elvidge et al., 2013), and the general lighting pattern of different urban land types remain similar to that of peak hours (Estrada-García et al., 2016; Li et al., 2020a). It is still reasonable, or even the best choice currently, to use VIIRS data for representing changes in urban land cover (Levin et al., 2020; Zhao et al., 2020b) and land use intensity (Levin and Zhang, 2017; Stokes and Seto, 2019), especially at a large spatial scale.

Although there are two coarse-resolution NTL datasets, DMSP-OLS and VIIRS, our study only applied to VIIRS time series. The main reason is that DMSP-OLS has no onboard calibration system and is also incompatible with VIIRS due to great gaps in sensor performance (Elvidge et al., 2013). Even though few methods have been proposed recently to harmonize DMSP-OLS and VIIRS (Zhao et al., 2020b; Zheng et al., 2019), they more or less rely on either certain assumptions or subjective operations. These issues will bring uncertainties to urban land change characterization and confound our analysis. Nevertheless, in future studies it is well worth incorporating the harmonized NTL time series and our proposed method to reveal long-term urban land changes of global megacities.

## 7. Conclusions

This research developed an effective method to characterize urban land changes in 30 global megacities. The proposed Logistic-Harmonic model, with the initial parameter estimation, created a robust

performance in fitting monthly VIIRS time series. We proposed a new classification scheme by using the modelling result and the extracted temporal features to produce monthly built-up areas maps, and to disentangle urban land change types. Our proposed method yielded a satisfying overall accuracy when assessed against ground truth reference generated by visual interpretation (95%) or GHSL (91%). The results demonstrated the superiority of temporal features over spectral features for classification of urban built-up areas. This superiority was found especially prominent in highly heterogeneous regions. In addition to the high classification accuracy, our method also greatly improved temporal consistency of the maps and classification efficiency. Urban land changes were found in 51% of built-up pixels. Urban land use changes, mostly urban land use intensification, contributed to an unexpectedly dominant proportion (96%) of total urban changes. The megacities in developing countries were observed to undergo through a wider extent and higher magnitude of urban land change, as well as a larger proportion of land use intensification, than the megacities of developed countries.

There are several issues worth further investigations. The upcoming Black Marble Product (VNP46A2) addresses many inherent problems of VIIRS data by implementing a series of corrections, including BRDF, atmospheric, stray light and lunar correction. The high-quality VNP46A2 data have a great potential to incorporate with the proposed method and to provide a better insights into global urban land changes (Román et al., 2018). In addition, the Logistic-Harmonic model could be improved to achieve a better modelling result in multi-stage urbanization, seasonality and special events. For instance, Mann-Kendall analysis and corrected Akaike Information Criterion (AICc) can be incorporated into a piece-wise logistic model to detect multi-stage urbanization. Finally, the applicability of our method should be further examined with cities of different sizes, geographical settings and stages, and in a longer temporal context.

## Declaration of Competing Interest

The authors declare that they have no known competing financial interests or personal relationships that could have appeared to influence the work reported in this paper.

## Acknowledgements

This study is supported in part by China Scholarship Council (Grant No. 201806320144), Academic Award for Outstanding Doctoral Candidate of Zhejiang University (Grant No. 2018092), IndianaView Student Scholarship Award from IndianaView Consortium (USGS), and Natural Science Foundation of China (Grant No. 41971236).

## Appendix A. Supplementary data

Supplementary data to this article can be found online at <https://doi.org/10.1016/j.isprsjprs.2021.01.002>.

## References

- Dou, Y., Liu, Z., He, C., Yue, H., 2017. Urban Land Extraction Using VIIRS Nighttime Light Data: An Evaluation of Three Popular Methods. *Remote Sensing* 9 (2), 175. <https://doi.org/10.3390/rs9020175>.
- Elvidge, C., Baugh, K., Zhizhin, M., & Hsu, F.-C. (2013). Why VIIRS data are superior to DMSP for mapping nighttime lights. *Proceedings of the Asia-Pacific Advanced Network*, 35(0), 62. doi:10.7125/apan.35.7.
- Elvidge, C., Baugh, K., Zhizhin, M., Hsu, F.C., Ghosh, T., 2017. VIIRS night-time lights. *Int. J. Remote Sensing* 38 (21), 5860–5879. <https://doi.org/10.1080/01431161.2017.1342050>.
- Esch, T., Heldens, W., Hirner, A., Keil, M., Marconcini, M., Roth, A., Strano, E., 2017. Breaking new ground in mapping human settlements from space – The Global Urban Footprint. *ISPRS J. Photogramm. Remote Sens.* 134, 30–42. <https://doi.org/10.1016/j.isprsjprs.2017.10.012>.
- Estrada-García, R., García-Gil, M., Acosta, L., Bará, S., Sanchez-de-Miguel, A., Zamorano, J., 2016. Statistical modelling and satellite monitoring of upward light

- from public lighting. *Light. Res. Technol.* 48 (7), 810–822. <https://doi.org/10.1177/1477153515583181>.
- GaWC. (2018). The World According to GaWC 2018-Classification of cities 2018. Retrieved from <https://www.lboro.ac.uk/gawc/world2018link.html>.
- Gómez, C., White, J.C., Wulder, M.A., 2016. Optical remotely sensed time series data for land cover classification: A review. *ISPRS J. Photogrammetry Remote Sensing* 116, 55–72. <https://doi.org/10.1016/j.isprsjprs.2016.03.008>.
- Griggs, D., Stafford-Smith, M., Gaffney, O., Rockström, J., Öhman, M.C., Shyamsundar, P., Noble, I., 2013. Policy: Sustainable development goals for people and planet. *Nature* 495 (7441), 305.
- Imhoff, M.L., Lawrence, W.T., Stutzer, D.C., Elvidge, C.D., 1997. A technique for using composite DMSP/OLS “city lights” satellite data to map urban area. *Remote Sens. Environ.* 61 (3), 361–370. Retrieved from <Go to ISI>://WOS:A1997XN25300003.
- Kennedy, R.E., Yang, Z., Cohen, W.B., 2010. Detecting trends in forest disturbance and recovery using yearly Landsat time series: 1. LandTrendr — Temporal segmentation algorithms. *Remote Sens. Environ.* 114 (12), 2897–2910. <https://doi.org/10.1016/j.rse.2010.07.008>.
- Kuechly, H.U., Kyba, C.C.M., Ruhtz, T., Lindemann, C., Wolter, C., Fischer, J., Höcker, F., 2012. Aerial survey and spatial analysis of sources of light pollution in Berlin, Germany. *Remote Sensing Environment* 126, 39–50. <https://doi.org/10.1016/j.rse.2012.08.008>.
- Levin, N., 2017. The impact of seasonal changes on observed nighttime brightness from 2014 to 2015 monthly VIIRS DNB composites. *Remote Sensing Environment* 193, 150–164. <https://doi.org/10.1016/j.rse.2017.03.003>.
- Levin, N., Kyba, C.C.M., Zhang, Q., de Miguel, A.S., Roman, M.O., Li, X., Elvidge, C.D., 2020. Remote sensing of night lights: A review and an outlook for the future. *Remote Sensing Environment* 237. <https://doi.org/10.1016/j.rse.2019.111443>.
- Levin, N., Zhang, Q., 2017. A global analysis of factors controlling VIIRS nighttime light levels from densely populated areas. *Remote Sens. Environ.* 190, 366–382. <https://doi.org/10.1016/j.rse.2017.01.006>.
- Li, M., Koks, E., Taubenboeck, H., van Vliet, J., 2020a. Continental-scale mapping and analysis of 3D building structure. *Remote Sens. Environ.* 245 <https://doi.org/10.1016/j.rse.2020.111859>.
- Li, S., Dragicevic, S., Castro, F.A., Sester, M., Winter, S., Coltekin, A., Cheng, T., 2016. Geospatial big data handling theory and methods: A review and research challenges. *ISPRS J. Photogrammetry Remote Sensing* 115, 119–133. <https://doi.org/10.1016/j.isprsjprs.2015.10.012>.
- Li, X., Levin, N., Xie, J., Li, D., 2020b. Monitoring hourly night-time light by an unmanned aerial vehicle and its implications to satellite remote sensing. *Remote Sensing Environment* 247. <https://doi.org/10.1016/j.rse.2020.111942>.
- Liu, Z., He, C., Zhang, Q., Huang, Q., Yang, Y., 2012. Extracting the dynamics of urban expansion in China using DMSP-OLS nighttime light data from 1992 to 2008. *Landscape Urban Planning* 106 (1), 62–72. <https://doi.org/10.1016/j.landurbplan.2012.02.013>.
- Long, Y., Wu, K., 2016. Shrinking cities in a rapidly urbanizing China. *Environment and Planning A* 48 (2), 220–222.
- Mahatta, R., Mahendra, A., Seto, K.C., 2019. Building up or spreading out? Typologies of urban growth across 478 cities of 1 million+. *Environ. Res. Lett.* 14 (12) <https://doi.org/10.1088/1748-9326/ab59bf>.
- Pesaresi, M., Huadong, G., Blaes, X., Ehrlich, D., Ferri, S., Gueguen, L., Lu, L., 2013. A global human settlement layer from optical HR/VHR RS data: concept and first results. *IEEE J. Selected Topics Applied Earth Observations Remote Sensing* 6 (5), 2102–2131.
- Román, M.O., Stokes, E.C., Shrestha, R., Wang, Z., Schultz, L., Carlo, E.A.S., Kalb, V., 2019. Satellite-based assessment of electricity restoration efforts in Puerto Rico after Hurricane Maria. *PLoS ONE* 14 (6), e0218883.
- Román, M.O., Wang, Z., Sun, Q., Kalb, V., Miller, S.D., Molthan, A., Masuoka, E.J., 2018. NASA’s Black Marble nighttime lights product suite. *Remote Sens. Environ.* 210, 113–143. <https://doi.org/10.1016/j.rse.2018.03.017>.
- Sanchez de Miguel, A., Kyba, C.C.M., Zamorano, J., Gallego, J., Gaston, K.J., 2020. The nature of the diffuse light near cities detected in nighttime satellite imagery. *Sci. Rep.* 10 (1) <https://doi.org/10.1038/s41598-020-64673-2>.
- Satterthwaite, D., McGranahan, G., Tacoli, C., 2010. Urbanization and its implications for food and farming. *Philosophical transactions of the royal society B: biological sciences* 365 (1554), 2809–2820.
- Seto, K. C., Golden, J. S., Alberti, M., & Turner, B. L., 2nd. (2017). Sustainability in an urbanizing planet. *Proc Natl Acad Sci U S A*, 114(34), 8935–8938. doi:10.1073/pnas.1606037114.
- Seto, K.C., General, B., Hutyra, L.R., 2012. Global forecasts of urban expansion to 2030 and direct impacts on biodiversity and carbon pools. *Proc. Natl. Acad. Sci. U S A* 109 (40), 16083–16088. <https://doi.org/10.1073/pnas.1211658109>.
- Song, X.-P., Hansen, M.C., Stehman, S.V., Potapov, P.V., Tyukavina, A., Vermote, E.F., Townshend, J.R., 2018. Global land change from 1982 to 2016. *Nature* 560 (7720), 639–643. <https://doi.org/10.1038/s41586-018-0411-9>.
- Song, X., 2016. Characterizing themagnitude, timing and duration of urban growth from time series of Landsat-based estimates of impervious cover. *Remote Sensing Environment* 175, 1–13. <https://doi.org/10.1016/j.rse.2015.12.027>.
- Stokes, E.C., Seto, K.C., 2019. Characterizing urban infrastructural transitions for the Sustainable Development Goals using multi-temporal land, population, and nighttime light data. *Remote Sens. Environ.* 234 <https://doi.org/10.1016/j.rse.2019.111430>.
- United Nations. (2016). The world's cities in 2016, data booklet. In: United Nations. United Nations. (2018). World Urbanization Prospects: The 2018 Revision, Online Edition. Retrieved from <https://population.un.org/wup/Download/>.
- United Nations. (2019). World Population Prospects 2019, Online Edition. Retrieved from <https://population.un.org/wpp/>.
- van Vliet, J., Verburg, P.H., Grădinaru, S.R., Hersperger, A.M., 2019. Beyond the urban-rural dichotomy: Towards a more nuanced analysis of changes in built-up land. *Comput. Environ. Urban Syst.* 74, 41–49. <https://doi.org/10.1016/j.compenvurbsys.2018.12.002>.
- Verbesselt, J., Hyndman, R., Zeileis, A., Culvenor, D., 2010. Phenological change detection while accounting for abrupt and gradual trends in satellite image time series. *Remote Sens. Environ.* 114 (12), 2970–2980. <https://doi.org/10.1016/j.rse.2010.08.003>.
- Vogelmann, J.E., Gallant, A.L., Shi, H., Zhu, Z., 2016. Perspectives on monitoring gradual change across the continuity of Landsat sensors using time-series data. *Remote Sens. Environ.* 185, 258–270. <https://doi.org/10.1016/j.rse.2016.02.060>.
- Xiao, P., Wang, X., Feng, X., Zhang, X., Yang, Y., 2014. Detecting China's Urban Expansion Over the Past Three Decades Using Nighttime Light Data. *IEEE J. Selected Topics Appl. Earth Observations Remote Sensing* 7 (10), 4095–4106. <https://doi.org/10.1109/jstARS.2014.2302855>.
- Xie, Y., Weng, Q., 2017. Spatiotemporally enhancing time-series DMSP/OLS nighttime light imagery for assessing large-scale urban dynamics. *ISPRS J. Photogrammetry Remote Sensing* 128, 1–15. <https://doi.org/10.1016/j.isprsjprs.2017.03.003>.
- Xie, Y., Weng, Q., Fu, P., 2019. Temporal variations of artificial nighttime lights and their implications for urbanization in the conterminous United States, 2013–2017. *Remote Sensing Environment* 225, 160–174. <https://doi.org/10.1016/j.rse.2019.03.008>.
- Xu, T., Ma, T., Zhou, C., Zhou, Y., 2014. Characterizing Spatio-Temporal Dynamics of Urbanization in China Using Time Series of DMSP/OLS Night Light Data. *Remote Sensing* 6 (8), 7708–7731. <https://doi.org/10.3390/rs6087708>.
- Yang, X., Ruby Leung, L., Zhao, N., Zhao, C., Qian, Y., Hu, K., Chen, B., 2017. Contribution of urbanization to the increase of extreme heat events in an urban agglomeration in east China. *Geophys. Res. Lett.* 44 (13), 6940–6950. <https://doi.org/10.1002/2017gl074084>.
- Ye, Y., Deng, J., Huang, L., Zheng, Q., Wang, K., Tong, C., Hong, Y., 2020. Modeling and Prediction of NPP-VIIRS Nighttime Light Imagery Based on Spatiotemporal Statistical Method. *IEEE Transactions Geoscience Remote Sensing* 1–13. <https://doi.org/10.1109/TGRS.2020.3011695>.
- Zhang, Q., Schaaf, C., Seto, K.C., 2013. The Vegetation Adjusted NTL Urban Index: A new approach to reduce saturation and increase variation in nighttime luminosity. *Remote Sensing Environment* 129, 32–41. <https://doi.org/10.1016/j.rse.2012.10.022>.
- Zhao, M., Zhou, Y., Li, X., Cheng, W., Zhou, C., Ma, T., Huang, K., 2020a. Mapping urban dynamics (1992–2018) in Southeast Asia using consistent nighttime light data from DMSP and VIIRS. *Remote Sens. Environ.* 248 <https://doi.org/10.1016/j.rse.2020.111980>.
- Zhao, N., Cao, G., Zhang, W., Samson, E.L., 2018a. Tweets or nighttime lights: Comparison for preeminence in estimating socioeconomic factors. *ISPRS J. Photogrammetry Remote Sens.* 146, 1–10. <https://doi.org/10.1016/j.isprsjprs.2018.08.018>.
- Zhao, N., Liu, Y., Hsu, F.-C., Samson, E.L., Letu, H., Liang, D., Cao, G., 2020b. Time series analysis of VIIRS-DNB nighttime lights imagery for change detection in urban areas: A case study of devastation in Puerto Rico from hurricanes Irma and Maria. *Appl. Geogr.* 120 <https://doi.org/10.1016/j.apgeog.2020.102222>.
- Zhao, N., Zhang, W., Liu, Y., Samson, E.L., Chen, Y., Cao, G., 2018b. Improving Nighttime Light Imagery With Location-Based Social Media Data. *IEEE Transactions Geoscience Remote Sensing* 1–12. <https://doi.org/10.1109/tgrs.2018.2871788>.
- Zheng, Q., Weng, Q., Huang, L., Wang, K., Deng, J., Jiang, R., Gan, M., 2018. A new source of multi-spectral high spatial resolution night-time light imagery—JL1-3B. *Remote Sens. Environ.* 215, 300–312. <https://doi.org/10.1016/j.rse.2018.06.016>.
- Zheng, Q., Weng, Q., Wang, K., 2019. Developing a new cross-sensor calibration model for DMSP-OLS and Suomi-NPP VIIRS night-light imageries. *ISPRS J. Photogramm. Remote Sens.* 153, 36–47. <https://doi.org/10.1016/j.isprsjprs.2019.04.019>.
- Zheng, Q., Weng, Q., Wang, K., 2020. Correcting the Pixel Blooming Effect (PiBE) of DMSP-OLS nighttime light imagery. *Remote Sens. Environ.* 240 <https://doi.org/10.1016/j.rse.2020.111707>.
- Zhou, Y., Li, X., Asrar, G.R., Smith, S.J., Imhoff, M., 2018. A global record of annual urban dynamics (1992–2013) from nighttime lights. *Remote Sens. Environ.* 219, 206–220. <https://doi.org/10.1016/j.rse.2018.10.015>.
- Zhu, Z., 2017. Change detection using landsat time series: A review of frequencies, preprocessing, algorithms, and applications. *ISPRS J. Photogramm. Remote Sens.* 130, 370–384. <https://doi.org/10.1016/j.isprsjprs.2017.06.013>.
- Zhu, Z., Woodcock, C.E., 2014. Continuous change detection and classification of land cover using all available Landsat data. *Remote Sens. Environ.* 144, 152–171. <https://doi.org/10.1016/j.rse.2014.01.011>.
- Zhu, Z., Zhou, Y., Seto, K.C., Stokes, E.C., Deng, C., Pickett, S.T.A., Taubenböck, H., 2019. Understanding an urbanizing planet: Strategic directions for remote sensing. *Remote Sens. Environ.* 228, 164–182. <https://doi.org/10.1016/j.rse.2019.04.020>.